scientific reports

OPEN

Continuous-wave second-harmonic generation in the far-UVC pumped by a blue laser diode

Eric J. Stanton[1,2,3,6]✉, Peter Tønning[4,6]✉, Emil Z. Ulsig[4,5], Stig Calmar[4], Maiya A. Stanton[1], Simon T. Thomsen[4,5], Kevin B. Gravesen[4,5], Peter Johansen[4] & Nicolas Volet[4,5]

Far-UVC light in the wavelength range of 200–230 nm has attracted renewed interest because of its safety for human exposure and effectiveness in inactivating pathogens. Here we present a compact solid-state far-UVC laser source based on second-harmonic generation (SHG) using a low-cost commercially-available blue laser diode pump. Leveraging the high intensity of light in a nanophotonic waveguide and heterogeneous integration, our approach achieves Cherenkov phase-matching across a bonded interface consisting of a silicon nitride (SiN) waveguide and a beta barium borate (BBO) nonlinear crystal. Through systematic investigations of waveguide dimensions and pump power, we analyze the dependencies of Cherenkov emission angle, conversion efficiency, and output power. Experimental results confirm the feasibility of generating far-UVC, paving the way for mass production in a compact form factor. This solid-state far-UVC laser source shows significant potential for applications in human-safe disinfection, non-line-of-sight free-space communication, and deep-UV Raman spectroscopy.

Over the past decade, extensive research has substantiated the safety of human exposure to far-UVC light (wavelengths from 200 nm to 230 nm) and its effectiveness in inactivating diverse pathogens, including human coronaviruses[1–10]. These compelling findings underscore the immense potential of far-UVC sources in curtailing airborne viral transmission, thereby playing a crucial role in the containment of diseases like COVID-19 and averting future pandemics. Additionally, far-UVC may be instrumental to improve yields in farming and pharmaceutical industries[11–13]. Previous studies have primarily investigated the disinfection and interactions of food, livestock, and pathogens with longer wavelengths (250–270 nm), which is unsafe for direct human exposure. However, employing human-safe far-UVC in these applications offers a notable advantage. By helping to eliminate contaminants, far-UVC could bring about additional societal benefits by enhancing the quality of goods in food and drug supply chains and curbing disease outbreaks that stem from these industries[14–18]. Beyond disinfection, compact far-UVC light sources can simplify free-space communication systems by eliminating the need for pointing accuracy and stability[19]. The reduced solar background noise in this spectrum and a broad acceptance angle may enable non-line-of-sight links, potentially reducing both the cost and complexity of the overall system. Furthermore, far-UVC lasers are beneficial for Raman spectroscopy[20], as they provide greater detail and higher quality information about a sample than lasers at longer wavelengths. The higher photon energy increases the Raman scattering efficiency and reduces the fluorescence background in numerous materials.

Achieving widespread and strategic deployment of far-UVC sources demands substantial technological advancements in the field[21]. The current leading commercial technology for far-UVC disinfection is the krypton chloride (KrCl) excimer lamp, emitting ∼150 mW with a spectral peak at 222 nm[22]. These devices use high-voltage (>1 kV) radio-frequency discharges resulting in a large power consumption. Inherently, their footprint is large (cm size), and they require a filter to eliminate dangerous wavelengths longer than 230 nm. While the KrCl emission wavelength cannot be tuned, slightly shorter wavelengths are anticipated to be safer and more effective in pathogen elimination[23]. Since the intensity of the lamp depends on the excimer volume (∼1 cm^3), the emission is difficult to control and inefficiently coupled to an optical fiber.

An attractive solution to reduce size, weight, operating power, and cost is direct emission of far-UVC from a semiconductor material. The performance of light-emitting diodes (LEDs) are progressing[24]. However, for laser

[1]EMode Photonix, Boulder, CO, USA. [2]National Institute of Standards and Technology, Boulder, CO, USA. [3]Department of Physics, University of Colorado, Boulder, CO, USA. [4]UVL A/S, Aarhus, Denmark. [5]Department of Electrical and Computer Engineering, Aarhus University, Aarhus, Denmark. [6]These authors contributed equally: Eric J. Stanton and Peter Tønning. ✉email: eric@emodephotonix.com; pto@uvmedico.com

diodes, the shortest emission wavelength to date is >270 nm[25], and fundamental obstacles remain that could potentially limit lifetime, efficiency, and output power.

We propose to convert light from a continuous-wave (CW) blue laser diode to the far-UVC using second-harmonic generation (SHG) in a waveguide, as depicted in Fig. 1a. (This figure is an artistic rendering; refer to the Results section for experiment details.) This approach leverages decades of research on GaN emitters for lighting[26,27] and incorporates recent advances in nanophotonic waveguide manufacturing[28,29]. The benefits of this approach include a low-voltage power supply, the low-cost and high-availability of blue laser diodes, wavelength flexibility, and the potential for low-cost fabrication with wafer-scale semiconductor manufacturing.

Beta barium borate (BBO) is commonly used for second-harmonic generation to the UV[30]. This is thanks to its broad transparency range, large nonlinearity and a shorter phase-matching cut-off wavelength compared to other nonlinear crystals[31,32]. A relatively compact demonstration with an external-cavity diode laser (ECDL) pump at 445 nm achieved far-UVC using bulk BBO, though with low conversion efficiency (∼0.01 % for 1.4 W pump)[33]. Recent advancements using resonant cavities showed improved efficiency with 13 % conversion from a 200 mW pump and 34 % conversion using cascaded SHG from a 1.6 W pump, both producing signals at ∼229 nm[34,35]. However, these systems require complex bulk optics for implementation.

Another approach for frequency conversion to the far-UVC involves a pulsed pump source for optical parametric oscillation and SHG. Demonstrations achieved 16.2 % efficiency from a 1.2 mJ pump, generating pulses at 222 nm wavelength[36]. Compressed pulses were also used in He-filled hollow capillary fibers, achieving 3.6 % conversion from 0.2 mJ pulses[37]. Pulse-pumping offers higher conversion efficiency but requires more complex and larger pump laser systems.

SHG in BBO waveguides was demonstrated at 266 nm wavelength with negligible walk-off and achieved 0.05 % conversion efficiency from a 670 mW pump[38]. However, phase-matching was limited to the bulk phase-matching angle, not utilizing the dispersion properties of the waveguide.

Our approach uses Cherenkov phase-matching[39] across a bonded interface, showcased in Fig. 1a,b, with a scanning electron micrograph in Fig. 1c. Blue pump light propagates in a waveguide, creating an evanescent field in a nonlinear crystal directly bonded to the waveguide core. This heterogeneous platform enables far-UVC generation without any interaction of the signal light with the waveguide core that guides the pump. Combining the precision and scalability of Si nanophotonics with the high nonlinearity and low loss of a bulk crystal is the key to achieving high conversion efficiency and stable operation.

Results

This work showcases experimental demonstrations of a heterogeneous photonic chip generating far-UVC with SHG from a blue diode laser. It is complemented by novel simulation results for the frequency converter chip design.

Numerical simulation and analysis

Phase-matching is found for various SiN waveguide heights and widths (Fig. 2a), with predicted Cherenkov angle values ranging from zero to ∼16°. In regions with large waveguide width and height, phase-matching collapses. The Cherenkov angle is close to zero along this boundary and generally increases for smaller widths and heights away from the boundary cut-off condition. While having the Cherenkov angle close to zero facilitates a low-angle emission at the BBO output facet, this work focuses on optimizing the conversion efficiency, irrespective of the Cherenkov angle.

The strength of the nonlinear interaction, independent of propagation loss, is observed by $\iint \kappa_\omega \, d\theta \, d\phi$ (as described in "Methods"), and is plotted in Fig. 2b. The results indicate that narrower and thicker waveguides provide a stronger frequency conversion. However, the realized frequency conversion takes into account the
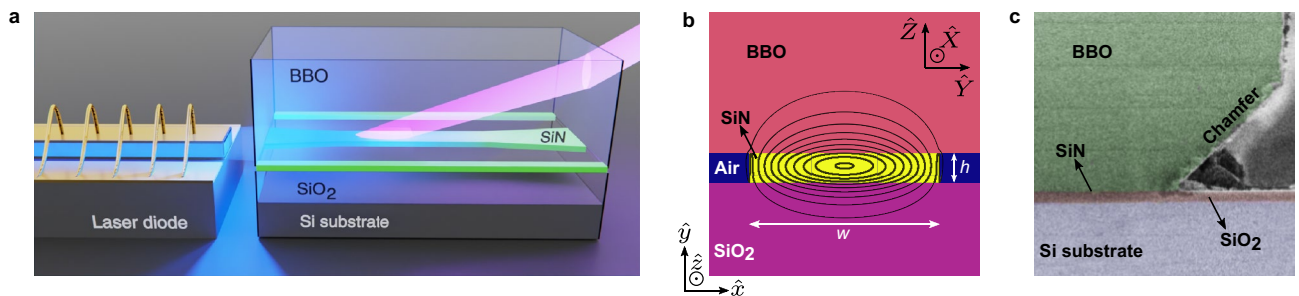
Figure 1. (**a**), Schematic of chip-to-chip edge coupling concept between a laser diode and the frequency converter showing the far-UVC generated at an angle above the waveguide core. (**b**), Waveguide cross-section schematic showing the BBO nonlinear crystal bonded to the SiN waveguide core of width w and thickness h. The Si substrate (not shown in this cross-section) is located below the SiO₂ lower cladding. Geometrical axes $\hat{x}$, $\hat{y}$ and $\hat{z}$ are shown, as well as crystal $\hat{X}$ axes $\hat{Y}$, and $\hat{Z}$ of BBO. Contour lines show the simulated $\hat{x}$-polarized electric field profile of the fundamental TE mode at a wavelength of 445 nm. The SiN core guides the mode with a confinement of 58 %, and a significant portion of the evanescent field (26 %) overlaps with the BBO. (**c**) Scanning electron micrograph showing the BBO crystal directly bonded to the SiN waveguide, with the SiO₂ lower cladding and the Si substrate. Edges of the BBO sample are chamfered for mechanical stability.
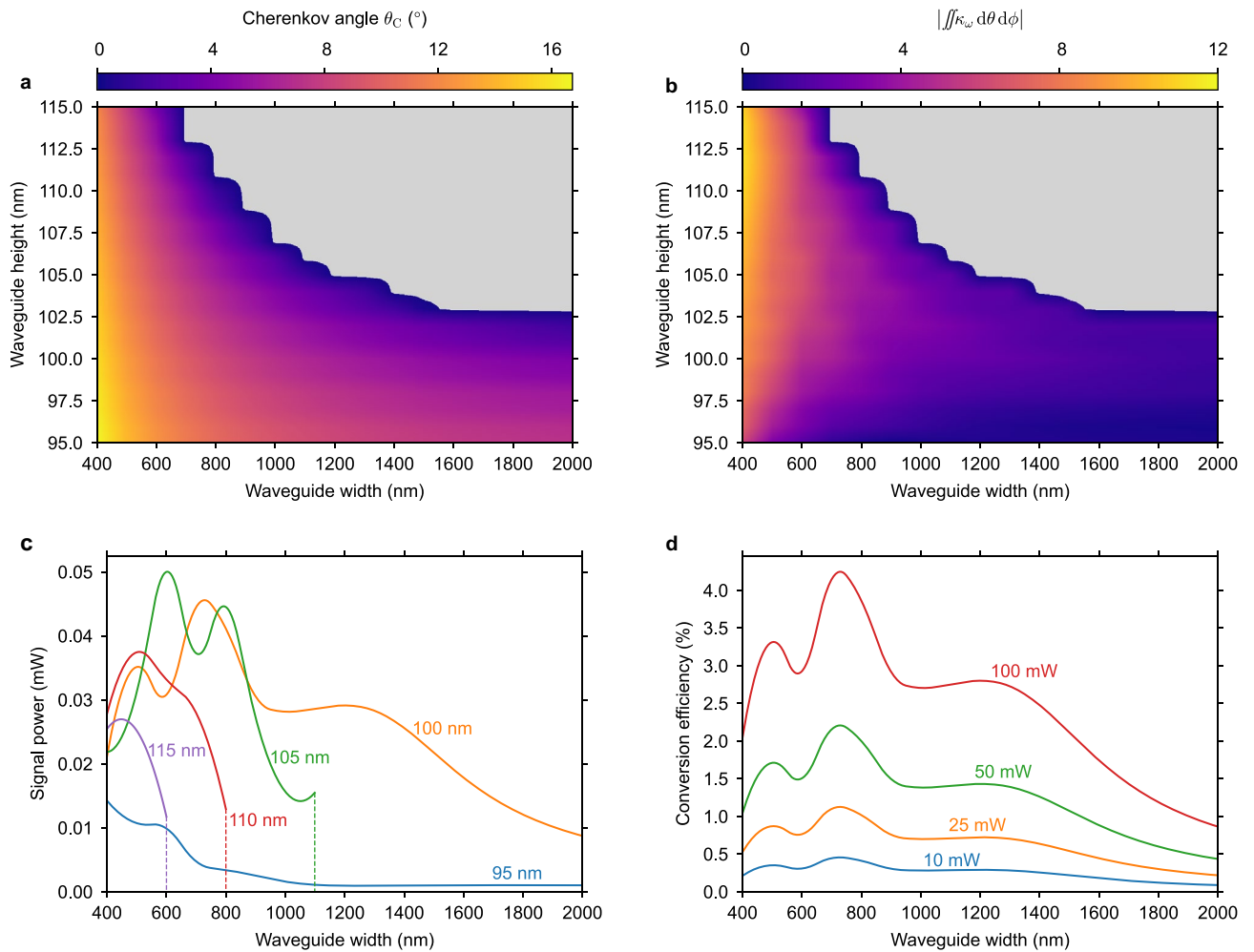
Figure 2. (**a**), Cherenkov angle simulated for the BBO/SiN hybrid waveguide for various thicknesses and widths of the SiN waveguide core. (**b**), Cherenkov nonlinear coupling parameter in a BBO/SiN waveguide as a function of the SiN core height and width. (**c**), Trends of the signal power with waveguide width for various waveguide heights as annotated on the plot for a pump power of 50 mW. (**d**), Trends of the conversion efficiency with waveguide width for various pump powers as annotated on the plot for a waveguide height of 100 nm.

losses, resulting in an optimal point for the SiN geometry, as propagation losses are inversely proportional to the waveguide width. Figure 3a shows the simulated propagation loss contribution from interfacial scattering and the sum of scattering and absorption losses in the SiN. Notably, measurements of the propagation loss align well with the predicted total loss values for the measured widths ranging from 500 to 2500 nm. From these data, the signal power and the conversion efficiency are predicted for selected waveguide heights (95 nm to 115 nm). Figure 2c shows the signal power trend with waveguide width for each height, with 100 nm being the preferred height due to its large peak value and broad phase-matching range. In Fig. 2d, the conversion efficiency is presented as a percentage of the pump power for this height at various pump powers. The on-chip pump power of 100 mW achieves a maximum efficiency of ∼4 %.

Figure 4a illustrates the signal power generated along the propagation of the pump waveguide, while Fig. 4b plots the signal and pump powers along z. The initial section of the waveguide experiences faster pump to signal conversion (indicated by the dashed grey line in Fig. 4b) due to the attenuation of pump light by propagation loss. Additionally, the ray diagram in Fig. 4a illustrates the output beam realization during the experiment. The larger-than-anticipated Cherenkov angle results in the signal reflecting from the top of the chip, leading to two emission beams, both downward and upward. This unexpected behavior is partly due to fabrication tolerance on the SiN layer thickness, resulting in a 98 nm thick layer instead of the targeted 100 nm. Furthermore, the BBO chip thickness was reduced due to an additional polishing step on the top surface to aid the coupling procedure with a microscope view. The azimuthal radiation profile, as shown in the inset of Fig. 4b, exhibits a local minimum at $\phi = 0$ attributed to the aspect ratio of the SiN waveguide. This effect can be mitigated by engineering a waveguide with a narrower width and thicker height.

While this device was designed for optimal operation with a 445 nm pump wavelength, other SiN geometries can support extremely broad-band phase-matching. For a waveguide thickness of 96 nm and a width of 2000 nm, Cherenkov phase-matching spans a continuous range of pump wavelengths from 400 nm to 1000 nm (Fig. 3b). While the trend ignores variation in propagation loss across this spectrum, it underscores the robustness of the
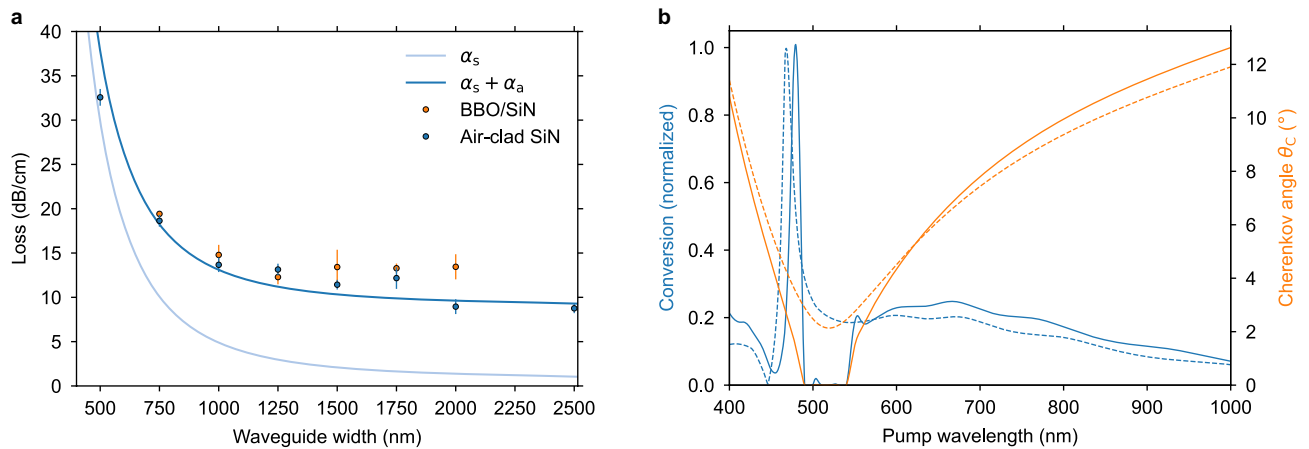
Figure 3. (**a**), Scattering loss (α_s) of TE-polarized modes in waveguides designed for Cherenkov phase-matching with 98 nm thick SiN, a sidewall roughness σ_{side} = 7 nm RMS, and a top surface roughness $\sigma_{surface}$ = 0.25 nm RMS. The absorption loss α_a is calculated from the material absorption loss of SiN scaled by the confinement factor, where α_{SiN} = 14 dB/cm. Measured propagation losses for the BBO/SiN and the air-clad SiN waveguides are plotted with data points, and error bars indicate the standard deviations of the measurement uncertainties. (**b**), Normalized conversion efficiency for SHG simulated across a broad range of pump wavelengths, plotted in blue on the left axis. The corresponding Cherenkov angle is plotted in orange on the right axis. Solid lines represent a waveguide with a 100 nm height and a 1500 nm width, which is the geometry optimized for SHG from a 445 nm wavelength pump. Dashed lines represent a waveguide with a 96 nm height and a 2000 nm width, showcasing a finite frequency conversion across the entire pump wavelength range of 400–1000 nm.
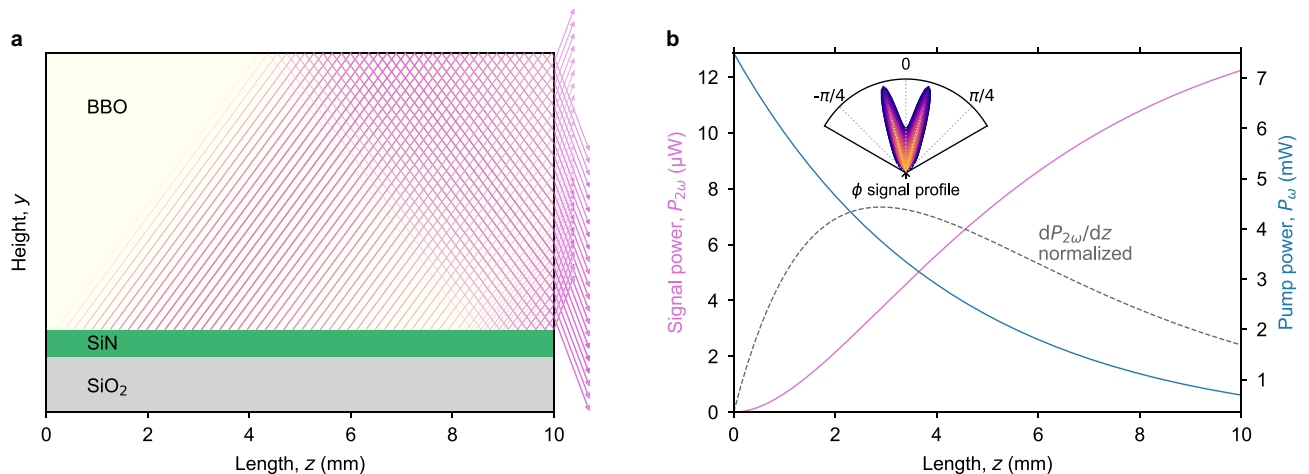
Figure 4. (**a**), Ray diagram of the signal generation in the BBO along the SiN waveguide. The ray width and transparency is scaled by the relative generated signal power per unit length, and the output at the right facet accounts for refraction. The SiN and SiO$_2$ layers are shown thicker than the actual layers for illustrative purposes. (**b**), The signal power $P_{2\omega}$ is generated along the propagation length z as the pump power P_ω depletes. The normalized differential of the signal power with the length z is shown with a dashed gray line, corresponding to the signal generation rays in **a**. The dependence of $P_{2\omega}$ on the azimuthal angle φ is shown in the inset.

Cherenkov approach, requiring no fine-tuning of refractive indices for phase-matching. Moreover, this discovery opens possibilities for the device's realization in other applications involving broadband frequency conversion.

Passive transmission

Firstly, we characterize devices comprising air-clad passive SiN waveguides without the bonded BBO to assess the relative contributions of scattering and absorption effects on propagation loss. The transmission of blue laser light is measured from straight waveguides to determine propagation and coupling losses. These results, along with the predicted trends, are plotted in Fig. 3a.

Subsequently, we measure blue light transmission with a BBO crystal bonded to the SiN waveguide layer. The TE-polarized light at 445 nm wavelength from a 2.0 μm wide waveguide exhibits a propagation loss of α_p =

13.4 ± 1.3 dB/cm, while the coupling loss to a lensed fiber is 11.0 dB. The presence of observable grain residues around the waveguide facet, arising from hybrid facet polishing, negatively impacts the coupling loss. This is evidenced by the trend of lower coupling losses for wider waveguides, where the light has less interaction with the SiN sidewall interface. However, wider waveguides result in increased relative coupling to higher-order modes, reducing the portion of light contributing to frequency conversion. To balance the effects of insertion loss, propagation loss, and single-mode propagation, there is an optimal waveguide width designed for the fundamental TE mode phase-matching. This optimal width is experimentally found in waveguides ranging from $1.0\,\mu$m and $2.0\,\mu$m in the following section.

SHG to the far-UVC

Far-UVC generation is measured with a blue laser diode pump and detecting the emitted light at various output angles from the BBO facet. During the experiments, the BBO crystal was not subject to heating, nor was it placed in an inert gas atmosphere. Figure 5a illustrates the output power dependence on the pump power using both ECDL and Fabry-Perot (FP) pump lasers at 445 nm, as shown in Fig. 5a (see "Methods" for details on laser sources used and a discussion about the calibrated output power of the far-UVC signal). Quadratic fits to both types of pump lasers result in coefficients of determination exceeding 98 %. Interestingly, the conversion efficiency from the FP laser appears unaffected by the expansion of lasing frequency modes when increasing the drive current. The observed difference in conversion efficiency is attributed to differences in the coupling loss of approximately 2.2 dB.

With a fixed pump power from a single-frequency laser at 445 nm wavelength, we measured the SHG output intensity for various emission angles in the subset of Fig. 5b. SHG light generated at the beginning of the waveguide can reflect at the top of the BBO chip and exit the BBO facet at the negative of the Cherenkov phasematched angle, with refraction at the exit facet. The same measurement was repeated with input wavelengths of 405 nm and 473 nm, corresponding to larger and smaller Cherenkov angles as predicted by simulations in Fig. 3b.

By changing the waveguide width, the effective index of the pump mode is varied, thereby modifying the Cherenkov angle and the conversion efficiency. In Fig. 5b the angle of maximum emission and the relative power at a fixed pump power is recorded as a function of the waveguide width. Although the far-UVC power is lower for waveguide widths of 750 nm and 1000 nm compared to wider widths, we expect this discrepancy to be attributed to facet coupling efficiency rather than a trend in the conversion efficiency. The trend in the Cherenkov angle predicted by simulations in Fig. 2 is confirmed with an additional offset.

Beyond the single axis distribution obtained from the goniometer, the far-field is further explored using a UV camera. A schematic of the setup with the camera placement and projection screens (described in "Methods") is displayed in Fig. 6 along with images captured of the screen positioned $\sim$20 cm from the chip. From Fig. 6 both upward and downward emission lobes are evident, with the lower emission significantly more intense, as explained from the geometrical considerations in Fig. 4. We also observe that Cherenkov phase-matching is achieved for a range of azimuthal angles (ϕ).

Wavelength tuning and SFG

As shown in Fig. 5a, the frequency converter exhibits tolerance to significant wavelength shifts, attributed to the robustness of Cherenkov phase-matching. This characteristic enables tunability, a valuable feature for several key applications in the far-UVC domain. Figure 7a demonstrates the direct mapping from wavelength tuning of the blue pump laser to the corresponding SHG signal across the tuning range of the stabilized diode laser.

The spectral tolerance of the frequency converter is further explored using different pump lasers to extend beyond the tuning range of the 445 nm laser. While the current design of the frequency converter chip is not
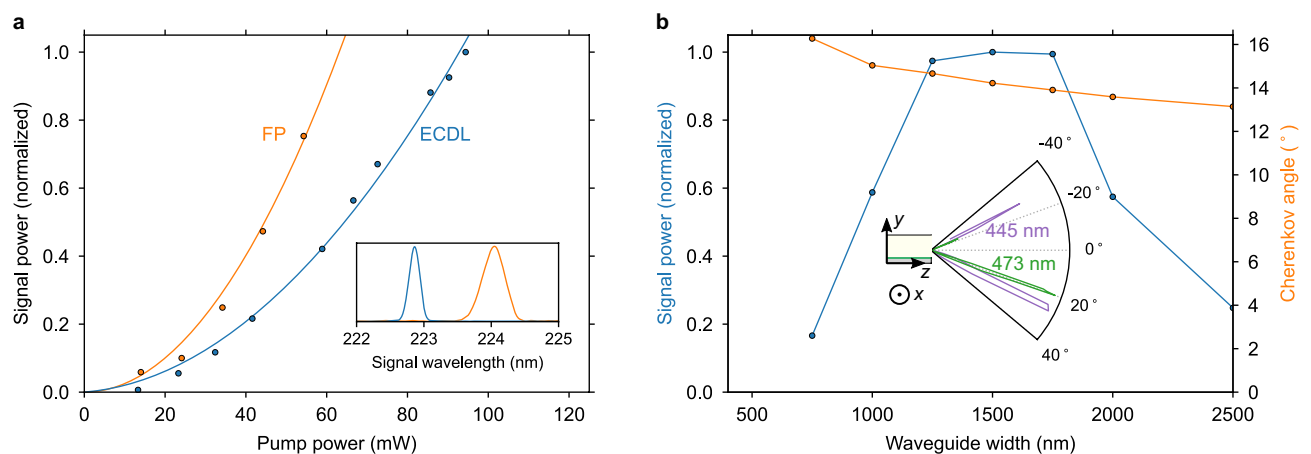

Figure 5. (**a**), Far-UVC power quadratic dependence on the off-chip pump power. The inset shows the far-UVC signal from an ECDL laser and an FP diode laser. (**b**), Waveguide width dependence on the far-UVC output intensity and the Cherenkov angle. The inset shows the angular dependence on the far-UVC output for pump wavelengths of 445 nm and 473 nm from a 1500 nm wide waveguide.

5
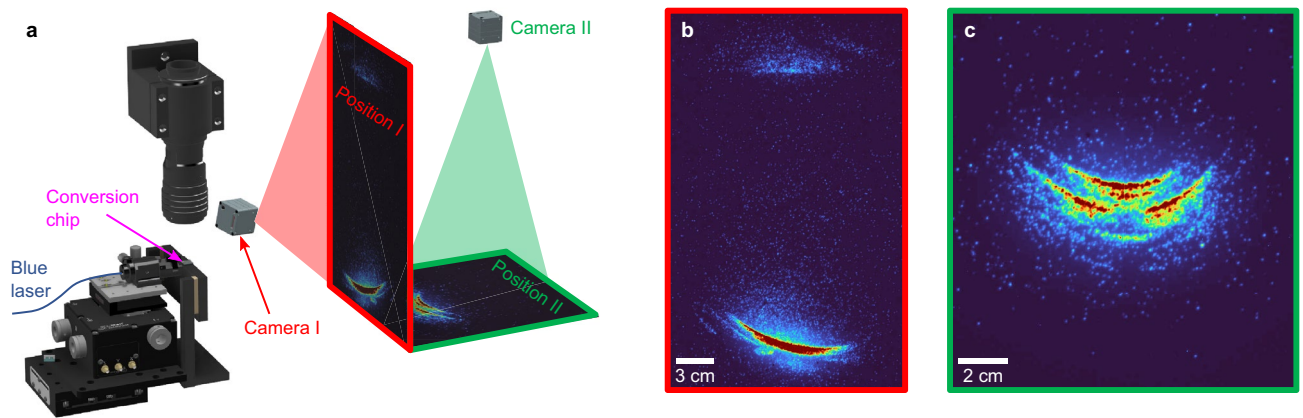
Figure 6. (**a**), Setup for capturing images of the far-field showing the placement and orientation of both camera and projection screen. The microscope shown above the conversion chip aids the alignment process of the lensed fiber to the chip. (**b**, **c**), Images of the far-UVC reflected off the projection screen, with the upper emission lobe less defined than the lower due to the multiple reflections through the BBO. A considerable spread in the azimuthal angle is observed as phase-matching is achieved with a range of Cherenkov angles.
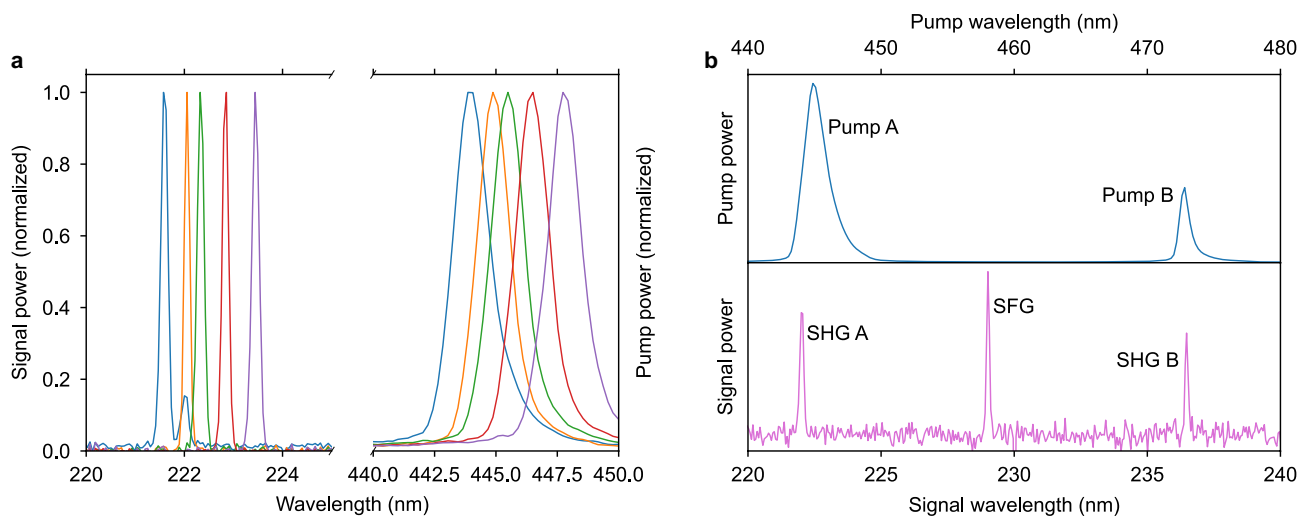
Figure 7. (**a**), Tuning the single-frequency pump laser produces a continuous sweep of far-UVC output wavelengths. (**b**), Using two pump lasers at respectively 445 nm and 473 nm, sum-frequency generation is demonstrated at 229.5 nm. The spectra, showing the normalized detected power, are recorded with two different optical spectrometers, the UV spectrometer having significantly higher resolution. As such the broader spectral appearance of the pump lasers is not their true spectral width as all spectra are under-sampled and merely reflect the resolution of the spectrometer.

optimized for pump wavelengths below 440 nm due to increased propagation loss in the SiN waveguides and lower conversion efficiency, slightly longer wavelengths support even higher conversion efficiency. This is demonstrated with a pump laser at 473 nm wavelength, as shown in Fig. 5b, where the Cherenkov angle is lower for the 473 nm pump as predicted in simulations, and the conversion efficiency is higher.

A far-UVC signal is also detected for a pump laser at 405 nm, as described in "Methods". However, due to higher losses indicating lower conversion efficiency, the output signal is very low, and thus, no spectrum was recorded at this wavelength. The output emission at 202.5 nm is observed at a steeper output angle compared to the longer far-UVC wavelengths. Most of the power lies in the upper emission lobe, as explained by Fig. 4a, where greater angles lead to double reflection of the signal generated in the first part of the chip.

Regardless, this result is significant because the pump wavelength of 405 nm is below the range for conventional phase-matching of SHG in bulk BBO[31,32]. In contrast, Cherenkov phase-matching can support efficient SHG well below 205 nm, which is promising for enabling unanticipated applications at wavelengths below 200 nm in the vacuum-UV.

By combining two pump lasers at 445 nm and 473 nm wavelengths, we can further explore the tolerance of phase-matching through sum-frequency generation (SFG). Both SHG and SFG are observed in Fig. 7b when each laser is coupled to the same waveguide on the frequency converter chip. Owing to the broadband phase-matching,

a single waveguide simultaneously supports SHG at 445 nm and 473 nm, with slightly different Cherenkov angles. Additionally, a SFG signal is produced with a wavelength of 229.5 nm.

Discussion

In conclusion, we have successfully demonstrated a solid-state far-UVC laser source using a chip-scale pump laser. This technology offers significant potential for mass production, benefiting from the extensive development of blue laser diodes. The broad phase-matching bandwidth is pivotal in achieving high-yield production with robust operation, ensuring the device's resilience against fabrication tolerances and environmental variations. As a result, pump sources like mass-produced FP laser diodes can be readily employed, facilitating the development process. The frequency converter utilizes standard materials and minimizes the material processing of BBO. This combination allows for a substantial reduction in size and price, thereby enabling the targeted high-volume application of disinfection.

Further, a compact far-UVC laser could drive other applications like non-line-of-sight communication, leveraging the drastic increase of scattering at shorter wavelengths[19] or Raman spectroscopy where excitation at wavelengths shorter than 250 nm alleviates autofluorescence[20]. Utilizing SFG, the spectral acceptance of pump sources enables compact realization of laser sources at a broad range of wavelengths. For example, combinations of compact diode lasers could be used to generate laser emission spanning the UV and visible spectra. We also envision that a frequency-comb pump source could be translated to the UV with this frequency converter device because of the broadband phase-matching.

The aspect ratio of the evanescent field of the pump mode in the BBO directly shapes the output signal beam profile. If the width-to-height ratio of this portion of the mode is too large, then the output beam gets a local minimum at the zero azimuthal angle, as shown in Fig. 4. In future work, we plan to engineer the output beam profile by tailoring the shape of the evanescent field in the BBO. This will enable optimization of the output beam for fiber coupling applications or a more uniform illumination for disinfection applications.

The main limiting factor in the presented work is the loss associated with input coupling and propagation through the SiN waveguide. As shown in Fig. 5, an increase in on-chip pump power has a significant impact on the signal power. Previous works demonstrating SiN waveguides with similar geometries show lower propagation losses of 5–7 dB/cm[40–42]. Other means of improvements lie in the material platform. Some evidence suggests lower loss from PECVD SiN[40]. Also, tantala could provide lower material absorption while maintaining a similar refractive index to SiN[43]. Gradual improvements in blue laser power densities are still seen from manufacturers, and pulsed operation could generate a higher power signal relevant for disinfection. The theory and architecture presented in this study provide multiple avenues for enhancing conversion efficiency, thereby increasing the power output of this compact solid-state far-UVC laser. Together, these advancements pave the way for far-UVC laser applications in non-line-of-sight free-space communication, Raman spectroscopy, and disinfection.

Methods

Design

SiN is used for the waveguide core layer to guide the blue pump light. BBO is used as the nonlinear crystal because of its large second-order nonlinearity, low loss in the far-UVC, and refractive indices compatible with Cherenkov phase-matching to SiN waveguides[30,44]. Figure 1b shows a schematic to define the waveguide width (w), height (h), the layer compositions, and the crystal axes relative to the device coordinate system. The BBO crystal is oriented to align d_{16} of the second-order nonlinear tensor to the TE-like pump mode in the SiN[45]. A contour profile of the $\hat{x}$-polarized electric field of the pump at 445 nm wavelength overlays the schematic. It has high confinement in the SiN core and a substantial overlap of the evanescent field with the BBO.

The first step in the design is to investigate geometries of SiN waveguides that support Cherenkov phase-matching to radiation modes in BBO bonded directly to SiN. With the propagation in the waveguide defined as the $\hat{z}$-direction, Cherenkov phase-matching occurs when the signal light propagates in a direction slightly elevated from the $\hat{z}$-direction towards the $\hat{y}$-direction, such that the $\hat{z}$-component of the phase velocity matches the pump phase velocity. The Cherenkov angle (θ_C) is the elevation angle θ of the signal wavevector relative to the SiN waveguide for the azimuthal angle of $\phi = 0$. This phase-matching condition occurs when:

$$n_\omega = n_{2\omega} \cos(\theta_C), \tag{1}$$

where n_ω is the effective refractive index of the guided pump mode and $n_{2\omega}$ is the refractive index the radiated signal light experiences in the nonlinear material. It is illustrated in Figs. 1a and 4a, and measured in Fig. 5a. Note that Cherenkov phase-matching can occur only when $n_{2\omega} \geqslant n_\omega$. This requirement dictates the materials that can be used for the core, cladding, and nonlinear regions of the Cherenkov SHG waveguide. It also creates a regime of operation for certain combinations of waveguide widths and heights such that n_ω is engineered to be smaller than $n_{2\omega}$.

The derivation for the Cherenkov SHG conversion efficiency follows the method proposed in[39], with some modifications to include propagation losses. The spatially dependent electric and magnetic fields (of either the pump or the signal) are assumed to take the form of:

$$\vec{\mathcal{E}}(x,y,z) = e^{ikz} Z(z) \vec{E}(x,y), \tag{2a}$$

$$\vec{\mathcal{H}}(x,y,z) = e^{ikz} Z(z) \vec{H}(x,y), \tag{2b}$$

where $\vec{E}$ and $\vec{H}$ are the electric and magnetic field components of the mode profile, assumed to be independent of z, and Z is a unitless complex function of z that accounts for nonlinear mode coupling. The term e^{ikz} with $k = \beta + i\alpha/2$ describes the propagation in the $\hat{z}$-direction through the associated component of the wavevector β and the power loss coefficient α. The pump mode profiles are calculated by a numerical simulation method[46]. The signal consists of a continuum of radiation modes that are best expressed analytically[47]. The approach taken by[39] for embedded channel waveguides is the approximation we use for this waveguide geometry. The $\hat{x}$-polarized electric field profile for TE-like radiation modes is calculated for an azimuthal range of: $-\pi/2 < \phi < \pi/2$.

Nonlinear coupling can be modeled with the following equation[48]:

$$\partial_z Z_\nu = i\frac{\omega_\nu}{4N_\nu}e^{-ik_\nu z}\iint_A \vec{P}_\nu^{\mathrm{NL}} \cdot \vec{E}_\nu^* \, \mathrm{d}x\,\mathrm{d}y, \tag{3}$$

with a normalization parameter (in units of power):

$$N_\nu = \frac{1}{2}\iint_A \Re\left[(\vec{E}_\nu \times \vec{H}_\nu^*) \cdot \hat{z}\right]\mathrm{d}x\,\mathrm{d}y, \tag{4}$$

where the integration is performed over a finite cross-sectional area A that completely encompasses the pump field. The nonlinear electrical polarizations are defined as $\vec{P}_\omega^{\mathrm{NL}} = 2\varepsilon_0 d\vec{v}_\omega$ for the pump and $\vec{P}_{2\omega}^{\mathrm{NL}} = \varepsilon_0 d\vec{v}_{2\omega}$ for the signal, ε_0 is the vacuum permittivity, d is the tensor representing the second-order nonlinearity of the material assuming Kleinman symmetry, and $\vec{v}$ is the corresponding complex vector of pump or signal electric field components. Next, the nonlinear coupling coefficients are calculated as a function of the elevation angle θ and of the azimuthal angle ϕ by:

$$\kappa_{2\omega} = \frac{\omega\varepsilon_0}{2N_{2\omega}}\iint_A (d\vec{v}_{2\omega}) \cdot \vec{E}_{2\omega}^* \, \mathrm{dx}\,\mathrm{dy}, \tag{5a}$$

$$\kappa_\omega = \frac{\omega\varepsilon_0}{2N_\omega}\iint_A (d\vec{v}_\omega) \cdot \vec{E}_\omega^* \, \mathrm{dx}\,\mathrm{dy}. \tag{5b}$$

Now the coupled-amplitude equations can be expressed as:

$$\partial_z Z_{2\omega} = iZ_\omega^2 \kappa_{2\omega} e^{-iz\Delta k}, \tag{6a}$$

$$\partial_z Z_\omega = iZ_\omega^* \iint Z_{2\omega}\kappa_\omega e^{(i\Delta k - \alpha_\omega)z} \, \mathrm{d}\theta\,\mathrm{d}\phi, \tag{6b}$$

where $\Delta k = k_{2\omega} - 2k_\omega$. Note that the signal amplitude $Z_{2\omega}$ is a function of θ and ϕ. The coupled-amplitude equations in Eq. 6 are solved numerically to find the signal output power $P_{2\omega}(z) = N_{2\omega}e^{-\alpha_{2\omega}z}\left|\iint Z_{2\omega}\,\mathrm{d}\theta\,\mathrm{d}\phi\right|^2$ in the radiated fields and the pump power $P_\omega(z) = N_\omega e^{-\alpha_\omega z}|Z_\omega|^2$ in the guided pump mode. The input pump power $P_{\omega,0}$ initializes the pump amplitude as $|Z_\omega(0)|^2 = P_{\omega,0}/N_\omega$, and the absence of an initial signal sets $Z_{2\omega}(0) = 0$. Note that the radiation fields and κ must be defined over the range of ϕ and a range of θ large enough to include all contributions.

Fabrication

Device fabrication starts with an oxidized Si wafer, on which a target of 100 nm SiN is formed by low-pressure chemical vapor deposition. The actual thickness of this layer is measured as 98 nm. Waveguides are patterned with deep-UV lithography and etched with inductively-coupled plasma reactive ion etching. Chips are singulated by dicing to a propagation length of 10 mm. BBO crystals are then grown and cut along the $\hat{X}$ crystal axis with a similar propagation length. The $\hat{Z}$ and $\hat{X}$ axes are polished. The SiN and BBO chips are directly bonded together after O_2 plasma activation, and the bond is strengthened with an anneal at 300 °C for 12 hours. Hybrid facets of Si and BBO are formed at the input and output of the waveguide by grinding and polishing to a single planar and smooth surface using a water-free polishing solution because BBO is hygroscopic. The facets are coated with MgF anti-reflective layers for the pump at the input side of the chip and for the signal at the output side.

Measurements

For all experiments a laser is coupled to the edge facet of the chip with lensed fibers. Polarization-maintaining (PM) fibers mounted on a 3-axis nanopositioning translation stage ensure close control of both polarization and spatial alignment. Detection equipment on the output side of the setup varies and is described for each measurement.

The following lasers are used to pump the nonlinear processes. A stabilized 445-nm diode laser (DLPro from Toptica) is used to pump SHG and SFG, and it is referenced as the ECDL. This laser has a manual tuning range of ~4 nm a maximum power in fiber of 95 mW and an instantaneous linewidth of 150 kHz. A fiber-coupled 445-nm FP diode laser (PL450B from Osram, packaged by OZ Optics) is used for SHG, and has a maximum power in fiber of 55 mW and a spectral width of ~1.5 nm corresponding to 10 to 15 longitudinal cavity modes. A fiber-coupled FP diode laser emitting around 405 nm (NDV4316 from Nichia, packaged by OZ Optics) is used for SHG, emitting a power of 45 mW in fiber and a ~1 nm spectral width, corresponding with 8 to 12 longitudinal cavity modes. Finally, a stabilized free-space diode laser at 473 nm with an intantaneous linewidth

<1 MHz (Cobolt08 from Hübner Photonics) is used for SHG and SFG. It is coupled to a single-mode PM fiber achieving 15 mW in the fiber.

For passive transmission measurements, PM lensed fibers are used for both the input and output coupling. Two techniques are used to discriminate the coupling loss from propagation loss. First the total power transmission is measured through detection on a fiber-coupled photodiode (S130VC from Thorlabs), secondly the scattered light intensity is measured along the waveguide from a microscope on top of the chip with a visible-light camera[49].

For characterizing the far-UVC signal from the frequency converter, the input coupling remains the same, while the output is collected using a custom designed 1D goniometer. The goniometer allows for mounting of different sensors recording the output at any output angle, vertically with reference to the waveguide at a fixed distance of 10 cm. For detection of the UVC signals either an optical spectrometer (Maya2000 Pro from Ocean Insight) or a photoemission detector (UVtron from Hamamatsu, with Ni electrode) is used. The photoemission detector gives a binary detection signal with very high sensitivity, allowing for investigations outside of the main emission lobe, however this detector has a low dynamic range. To measure the output angle θ, shown in Fig. 5b, the photoemission detector is mounted on the 1D goniometer. The limited dynamic range leads to saturation at the main emission lobe from the 445 nm pump laser. Due to its high directionality, lack of calibration, and limited dynamic range, the photoemission detector cannot be effectively mapped to a calibrated power-meter within this range. The spectrometer on the other hand has a linear intensity response, excellent dynamic range, but measures intensity in a small aperture of the input multi-mode fiber of 600 µm. The spectrometer has a resolution of 0.15 nm and covers a range of 165–275 nm, leaving it blind to the pump wavelengths in the blue (405–473 nm). The signal at 202.5 nm wavelength is only detected using the highly sensitive photoemission detector, whereas the other far-UVC signals are recorded both as spectra and with the photoemission detector.

Determining a calibrated measurement of the signal power has not yet been achieved. The significant coupling and propagation losses are accompanied by diffuse scattering of the blue light from the pump at intensities much higher than the far-UVC signal. Hence, a detector must have both very high sensitivity in the UV while having high suppression in the blue. By calibrating the spectrometer against a well known KrCl excimer source emitting at 222 nm, the irradiance from the frequency converter is estimated to be 0.17 µW/cm^2. This solitary measurement gives no direct value for total output power nor conversion efficiency as it constitutes a very localized intensity in a complex radiation pattern.

A projection screen made from highly UV reflective PTFE (POREX Virtek) is placed in front of the emission region, giving a diffuse reflection of the far-field at the position of the projection screen. The UV camera is highly selective in favor of the UV light over the visible. In combination with a band-pass filter centered at 220 nm, the camera setup becomes completely blind to the intense blue pump-laser, imaging only the far-UVC generated from the frequency conversion.

For the SFG measurement, the ECDL at 445 nm wavelength and the free-space laser at 473 nm wavelength are combined in a polarization-maintaining fiber splitter. By ensuring the polarization is aligned to the same axis at the fiber input, both lasers are coupled to the same waveguide in the frequency converter chip in TE polarization. To balance the coupling of the three generated UV signals, the angular position of the output spectrometer probe is selected as a compromise because the Cherenkov angle varies with the wavelength.

Data availability
The datasets generated during the current study are available from the corresponding author on reasonable request.

References
1. Buonanno, M. *et al.* Germicidal efficacy and mammalian skin safety of 222-nm UV light. *Radiat. Res.* **187**, 493–501 (2017).
2. Ponnaiya, B. *et al.* Far-UVC light prevents MRSA infection of superficial wounds in vivo. *PLoS ONE* **13**, e0192053 (2018).
3. Buonanno, M., Welch, D., Shuryak, I. & Brenner, D. J. Far-UVC light (222 nm) efficiently and safely inactivates airborne human coronaviruses. *Sci. Rep.* **10**, 1–8 (2020).
4. Kitagawa, H. *et al.* Effectiveness of 222-nm ultraviolet light on disinfecting SARS-CoV-2 surface contamination. *Am. J. Infect. Control* **49**, 299–301 (2021).
5. Ma, B. *et al.* Inactivation of coronaviruses and phage Phi6 from irradiation across UVC wavelengths. *Environ. Sci. Technol. Lett.* **8**, 425–430 (2021).
6. Ma, B., Gundy, P. M., Gerba, C. P., Sobsey, M. D. & Linden, K. G. UV inactivation of SARS-CoV-2 across the UVC spectrum: KrCl* excimer, mercury-vapor, and light-emitting-diode (LED) sources. *Appl. Environ. Microbiol.* **87**, e01532-21 (2021).
7. Glaab, J. *et al.* Skin tolerant inactivation of multiresistant pathogens using far-UVC LEDs. *Sci. Rep.* **11**, 1–11 (2021).
8. Sugihara, K. *et al.* One-year Ocular Safety Observation of Workers and Estimations of Microorganism Inactivation Efficacy in the Room Irradiated with 222-nm Far Ultraviolet-C Lamps (Photochem, Photobiol, 2022).
9. Blatchley, E. R. III. *et al.* Far UV-C radiation: An emerging tool for pandemic control. *Crit. Rev. Environ. Sci. Technol.* **53**, 733–753 (2023).
10. Welch, D. *et al.* No evidence of induced skin cancer or other skin abnormalities after long-term (66 week) chronic exposure to 222-nm far-UVC radiation. *Photochem. Photobiol.* **99**, 168–175 (2023).
11. Singh, H., Bhardwaj, S. K., Khatri, M., Kim, K.-H. & Bhardwaj, N. UVC radiation for food safety: An emerging technology for the microbial disinfection of food products. *Chem. Eng. J.* **417**, 128084 (2021).
12. Subedi, S., Koirala, S. & Chai, L. COVID-19 in farm animals: Host susceptibility and prevention strategies. *Animals* **11**, 640 (2021).
13. Ramos, C. C. R. *et al.* Use of ultraviolet-C in environmental sterilization in hospitals: A systematic review on efficacy and safety. *Int. J. Health Sci.* **14**, 52 (2020).
14. Grida, M., Mohamed, R. & Zaied, A. N. H. Evaluate the impact of COVID-19 prevention policies on supply chain aspects under uncertainty. *Transp. Res. Interdiscip. Perspect.* **8**, 100240 (2020).

15. Rowan, N. J. & Laffey, J. G. Challenges and solutions for addressing critical shortage of supply chain for personal and protective equipment (PPE) arising from Coronavirus disease (COVID19) pandemic-Case study from the Republic of Ireland. *Sci. Total Environ.* **725**, 138532 (2020).
16. Abdolazimi, O., Salehi Esfandarani, M., Salehi, M., Shishebori, D. & Shakhsi-Niaei, M. Development of sustainable and resilient healthcare and non-cold pharmaceutical distribution supply chain for COVID-19 pandemic: A case study. *Int. J. Logist. Manag.* **34**, 363–389 (2023).
17. Miranda, R. C. & Schaffner, D. W. Virus risk in the food supply chain. *Curr. Opin. Food Sci.* **30**, 43–48 (2019).
18. Rizou, M., Galanakis, I. M., Aldawoud, T. M. & Galanakis, C. M. Safety of foods, food supply chain and environment within the COVID-19 pandemic. *Trends Food Sci. Technol.* **102**, 293–299 (2020).
19. Cai, Q. *et al.* Progress on AlGaN-based solar-blind ultraviolet photodetectors and focal plane arrays. *Light Sci. Appl.* **10**, 94 (2021).
20. Hara, E. Detecting organics with Deep UV Raman and fluorescence spectroscopy. *Nat. Rev. Earth Environ.* **3**, 164 (2022).
21. Kneissl, M., Seong, T.-Y., Han, J. & Amano, H. The emergence and prospects of deep-ultraviolet light-emitting diode technologies. *Nat. Photon.* **13**, 233–244 (2019).
22. Eadie, E. *et al.* Far-UVC (222 nm) efficiently inactivates an airborne pathogen in a room-sized chamber. *Sci. Rep.* **12**, 4373 (2022).
23. Hessling, M., Haag, R., Sieber, N. & Vatter, P. The impact of far-UVC radiation (200–230 nm) on pathogens, cells, skin, and eyes–a collection and analysis of a hundred years of data. *GMS Hyg. Infect. Control* **16** (2021).
24. Knauer, A. *et al.* Strain induced power enhancement of far-UVC LEDs on high temperature annealed AlN templates. *Appl. Phys. Lett.* **122**, 011102 (2023).
25. Zhang, Z. *et al.* Key temperature-dependent characteristics of AlGaN-based UV-C laser diode and demonstration of room-temperature continuous-wave lasing. *Appl. Phys. Lett.* **121**, 222103 (2022).
26. Pimputkar, S., Speck, J. S. & DenBaars, S. P. Prospects for LED lighting. *Nat. Photon.* **3**, 180–182 (2009).
27. Behringer, M. & König, H. Blue high-power laser diodes-beam sources for novel applications: Overview and outlook. *PhotonicsViews* **17**, 60–63 (2020).
28. Blumenthal, D. J., Heideman, R., Geuzebroek, D., Leinse, A. & Roeloffzen, C. Silicon nitride in silicon photonics. *Proc. IEEE* **106**, 2209–2231 (2018).
29. Chanana, A. *et al.* Ultra-low loss quantum photonic circuits integrated with single quantum emitters. *Nat. Commun.* **13**, 7693 (2022).
30. Eimerl, D., Davis, L., Velsko, S., Graham, E. & Zalkin, A. Optical, mechanical, and thermal properties of barium borate. *J. Appl. Phys.* **62**, 1968–1983 (1987).
31. Kang, L. & Lin, Z. Deep-ultraviolet nonlinear optical crystals: concept development and materials discovery. *Light Sci. Appl.* **11**, 201 (2022).
32. Mutailipu, M. *et al.* Achieving the full-wavelength phase-matching for efficient nonlinear optical frequency conversion in $C(NH_2)_3BF_4$. *Nat. Photon.* 1–8 (2023).
33. Ruhnke, N. *et al.* Compact deep UV system at 222.5 nm based on frequency doubling of GaN laser diode emission. *IEEE Photon. Technol. Lett.* **30**, 289–292 (2018).
34. Foster, M. *et al.* Demonstration of a compact deep UV Raman spatial heterodyne spectrometer for biologics analysis. *J. Biophoton.* **15**, e202200021 (2022).
35. Kaneda, Y. *et al.* Continuous-wave, single-frequency 229 nm laser source for laser cooling of cadmium atoms. *Opt. Lett.* **41**, 705–708 (2016).
36. Luo, Q., Ma, J., Wang, M., Lu, T. & Zhu, X. All-solid-state far-UVC pulse laser at 222 nm wavelength for UVC disinfection. *Chin. Opt. Lett.* **21**, 011401 (2023).
37. Brahms, C. & Travers, J. C. Efficient and compact source of tuneable ultrafast deep ultraviolet laser pulses at 50 kHz repetition rate. *Opt. Lett.* **48**, 151–154 (2023).
38. Degl'Innocenti, R. *et al.* UV second harmonic generation at 266 nm in He^+ implanted β-BaB_2O_4 optical waveguides. *Opt. Express* **16**, 11660–11669 (2008).
39. Suhara, T., Morimoto, T. & Nishihara, H. General coupled-mode analysis of Cerenkov-radiation-type second-harmonic generation in channel and fiber waveguides. *IEEE J. Quantum Electron.* **29**, 525–537 (1993).
40. Sorace-Agaskar, C. *et al.* Versatile silicon nitride and alumina integrated photonic platforms for the ultraviolet to short-wave infrared. *IEEE J. Sel. Top. Quantum Electron.* **25**, 1–15 (2019).
41. Chauhan, N. *et al.* Ultra-low loss visible light waveguides for integrated atomic, molecular, and quantum photonics. *Opt. Express* **30**, 6960–6969 (2022).
42. Smith, J. A., Francis, H., Navickaite, G. & Strain, M. J. SiN foundry platform for high performance visible light integrated photonics. *Opt. Mater. Express* **13**, 458–468 (2023).
43. Spektor, G. *et al.* Universal visible emitters in nanoscale integrated photonics. *Optica* **10**, 871–879 (2023).
44. Tamošauskas, G. β-Barium Borate (BBO) Absorption in the 0.188-6.22 μm Range. arXiv preprint: 2111.01212 (2021).
45. Volet, N., Ulsig, E. Z., Degli-Eredi, I., Tønning, P. & Stanton, E. J. Walk-off effect in nonlinear crystals suitable for UVC generation. *Proc. SPIE* **11670**, 116701O (2021).
46. EMode (version 0.0.6-b4) [Software] from EMode Photonix. Available at emodephotonix.com
47. Papakonstantinou, I., James, R. & Selviah, D. R. Radiation- and bound-mode propagation in rectangular, multimode dielectric, channel waveguides with sidewall roughness. *J. Light. Technol.* **27**, 4151–4163 (2009).
48. Stegeman, G. I. & Seaton, C. T. Nonlinear integrated optics. *J. Appl. Phys.* **58**, R57–R78 (1985).
49. Daldosso, N. *et al.* Comparison among various Si_3N_4 waveguide geometries grown within a CMOS fabrication pilot line. *J. Lightwave Technol.* **22**, 1734–1740 (2004).

Acknowledgements

Author contributions

E.J.S, E.Z.U., P.J. and N.V. conceived the project. E.J.S., P.T., E.Z.U. and N.V. developed the theory. E.J.S., P.T. and E.Z.U. designed the structure and fabrication process. E.J.S., P.T., E.Z.U., S.C., M.A.S., S.T.T. and K.B.G. conducted the experiments. E.J.S., P.T., E.Z.U., S.T.T. and K.B.G. performed the data analysis. E.J.S. and P.T. wrote the manuscript with contributions from all authors. M.A.S. and N.V. supervised the project.

Competing interests

E.J.S. and M.A.S. are members of EMode Photonix. E.Z.U. and N.V. are co-founders of UVL A/S. All other authors declare that they do not have any competing interest.

Additional information

Correspondence and requests for materials should be addressed to E.J.S. or P.T.

Reprints and permissions information is available at www.nature.com/reprints.

Publisher's note Springer Nature remains neutral with regard to jurisdictional claims in published maps and institutional affiliations.